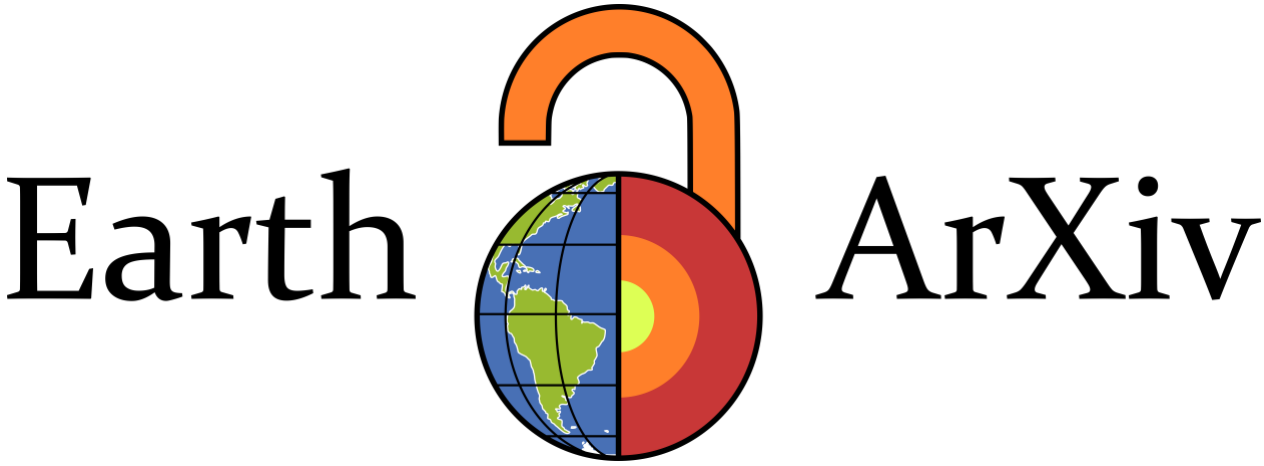


This is a non-peer-reviewed preprint submitted to EarthArXiv.

This manuscript has been submitted for publication in Environmental Fluid Mechanics. Please note the manuscript has yet to be formally accepted for publication. Subsequent versions of this manuscript may have slightly different content. If accepted, the final version of this manuscript will be available via the 'Peer-reviewed Publication DOI' link on the right-hand side of this webpage. Please feel free to contact any of the authors; we welcome feedback.

One-dimensional model equations for unsteady axisymmetric free-boundary potential flow in porous media

Carmine Di Nucci[1*†], Mohammad Afzal Shadab[2,3†], Piera Fischione[1†], Daniele Celli[1†], Davide Pasquali[1†], Marcello Di Risio[1†]

[1*]Environmental and Maritime Hydraulic Laboratory (LIam), Civil, Construction-Architectural and Environmental Engineering Department (DICEAA), University of L'Aquila, Piazzale Ernesto Pontieri, Monteluco di Roio, L'Aquila, 67100, Italy.

[2] Department of Civil and Environmental Engineering, Princeton University, Princeton, 08544, New Jersey, USA.

[3] Integrated GroundWater Modeling Center, Princeton University, Princeton, 08544, New Jersey, USA.

*Corresponding author(s). E-mail(s): carmine.dinucci@univaq.it;
Contributing authors: mashadab@princeton.edu; piera.fischione@univaq.it; daniele.celli@univaq.it; davide.pasquali@univaq.it; marcello.dirisio@univaq.it;
†These authors contributed equally to this work.

Abstract

This paper deals with the derivation of one-dimensional model equations for unsteady axisymmetric free-boundary potential flow in saturated, homogeneous and isotropic porous media. An approximation of the irrotational and solenoidal velocity field, obtained by means of a Picard iteration, is employed to derive a momentum equation accounting for vertical-flow effects. The model is completed by the one-dimensional continuity equation. The axisymmetric Cauchy integral relation is also derived. The model is applied to flow toward a fully penetrating well in a non-deformable porous medium with a horizontal impermeable bed, neglecting capillary-fringe effects. The resulting equations are numerically integrated to determine the free-boundary evolution, the flow-rate distribution, the water level in the well, and the seepage-face development. The numerical results

show satisfactory agreement with Boundary Integral Equation Method results available in the literature and with the VarSatFlow simulations under prescribed well-water-level conditions. The results indicate that the proposed model captures the main features of the transient flow; some differences occur near the well.

Keywords: Free boundary problem, potential flow, axisymmetric flow, one-dimensional model, porous media, seepage face

Article Highlights

- One-dimensional model equations are derived for unsteady axisymmetric free-boundary potential flow.
- The model accounts for vertical-flow effects and seepage-face development.
- The numerical results show satisfactory agreement with reference numerical solutions.

1 Introduction

Groundwater flow is involved in several problems concerning water supply and drainage in porous media. In unconfined aquifers, variations in the hydraulic conditions cause the saturated and unsaturated regions to evolve with time. Several numerical methods and computational tools are available to describe these processes [1, 2]. Nevertheless, simplified models remain of interest, since they can reproduce the main features of the flow with a reduced mathematical description. In particular, one-dimensional models accounting for effects neglected in classical approximations may provide a useful improvement while retaining a relatively simple formulation [3–5].

Motivated by these considerations, we address the derivation of one-dimensional model equations for unsteady axisymmetric potential flow in unconfined aquifers. The fluid is assumed incompressible and the porous medium homogeneous, isotropic, and non-deformable. A horizontal impermeable bed is considered. Neglecting capillary-fringe effects, the phreatic surface is identified with the free boundary of the flow domain.

The flow problem consists in finding the irrotational and solenoidal velocity field, the pressure field, and the time-dependent free-boundary position. The flow toward a fully penetrating well is considered as an application of the model. With reference to the fully penetrating well problem, the solution also requires the determination of the water level in the well and of the so-called seepage face, i.e., the surface of the well wall between the water level in the well and the free boundary in the porous medium [6].

A classical numerical approach for solving free-boundary problems is the Boundary Integral Equation Method (BIEM) [7–10]. The method is based on the solution of the Laplace equation for the velocity potential in the time-dependent flow domain, while the free-surface position is updated through the kinematic boundary condition. Other

classical numerical treatments are based on finite-element and finite-difference formulations [1, 11]. More recently, Shadab and Hesse [2] proposed a hyperbolic–elliptic PDE model and a conservative numerical method for gravity-dominated variably saturated groundwater flow, referred to as VarSatFlow.

An alternative to the direct numerical solution of the free-boundary problem is represented by approximate analytical and semi-analytical approaches, generally based on linearization of the free-surface boundary condition or on perturbation methods [12–14].

Within a one-dimensional framework, the classical solution approach is based on the Dupuit–Forchheimer approximation. Several approaches have been proposed to improve this approximation by taking into account vertical-flow effects and the inclination and curvature of the streamlines [3, 4, 15–17]. Further one-dimensional models also account for the seepage face [5, 18, 19]. Classical semi-analytical solutions for steady free-surface seepage through rectangular porous dams were developed by Polubarinova-Kochina [20]. More recently, Shadab et al. [21] provided a numerical implementation of the Polubarinova-Kochina solutions. Reduced formulations for unsteady free-surface flow, higher-order corrections to Dupuit-type descriptions, models that relax the Dupuit hypothesis, and numerical treatments of seepage-face boundary conditions can be found in [22–25]. The use of Picard iteration for deriving a second-order approximation of two-dimensional drainage flow has also been considered in [26]. The same iterative procedure, originally applied to open-channel potential flows by Matthew [27], has been considered in [28, 29].

In this paper, in order to derive one-dimensional model equations for unsteady axisymmetric free-boundary potential flow, we extend the Picard procedure developed in [18] for steady axisymmetric potential flow to the unsteady case. The resulting approximation of the irrotational and solenoidal velocity field is employed to obtain a one-dimensional momentum equation accounting for vertical-flow effects. The continuity equation is obtained directly from mass conservation.

The model equations are then applied to the flow toward a fully penetrating well. The Cauchy integral relation introduced in [5] for a rectangular porous domain is reformulated for axisymmetric geometry. For the fully penetrating well problem, this relation, together with the well mass-balance equation, completes the one-dimensional model. The equations are numerically integrated to determine the free-boundary evolution, the flow-rate distribution, the water level in the well, and the seepage-face development. The results are compared with reference numerical results available in the literature [10]. Under prescribed well-water-level conditions, the model results are compared with the VarSatFlow simulations.

The paper is organized as follows. Section 2 defines the free-boundary problem for the reference well configuration. Section 3 illustrates the Picard iteration. In Section 4 we derive the one-dimensional model equations, apply them to the pumping-well problem considered in [10], and compare the numerical results available in the literature with the model results. A comparison between the model results and the VarSatFlow simulations is also provided. The conclusions are discussed in Section 5. A derivation of the axisymmetric Cauchy integral relation is given in Appendix A, while the equivalence between the third Picard approximation and the corresponding truncation

of the long-wave expansion is shown in Appendix B. The details of the VarSatFlow formulation, discretization and saturation criterion are provided in Appendix C.

2 The free-boundary problem

To define the governing equations and boundary conditions, we consider the unsteady axisymmetric flow toward a fully penetrating well in a saturated, homogeneous, and isotropic porous medium (Figure 1). The porous medium is non-deformable and the fluid is incompressible. The horizontal impermeable bed is located at $z = 0$, while $z = h(r,t)$ denotes the free boundary, with r the radial coordinate. The well radius is denoted by r_w, and R is the external radius of the flow domain. The undisturbed water level is equal to H, while $h_w(t)$ denotes the water level in the well. Neglecting

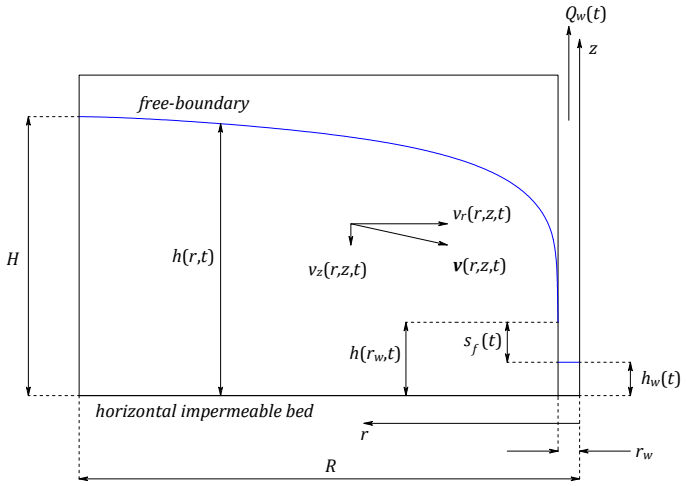


Fig. 1 Definition sketch.

capillary-fringe effects, the pressure on the free boundary is atmospheric and the free boundary coincides with the phreatic surface. The seepage-face height is defined as

$$s_f(t) = h(r_w, t) - h_w(t). \tag{1}$$

The axisymmetric velocity field $\boldsymbol{v}$ is irrotational and solenoidal. The radial velocity component $v_r(r,z,t)$ is assumed positive toward the well, while the vertical velocity component $v_z(r,z,t)$ is positive upward. In the range of validity of Darcy's law, the velocity components are given by

$$v_r = k\frac{\partial \phi}{\partial r}, \tag{2}$$

and

$$v_z = -k\frac{\partial \phi}{\partial z}, \tag{3}$$

where k is the hydraulic conductivity and

$$\phi = z + \frac{p}{\rho g} \tag{4}$$

is the potential function, with p pressure, ρ fluid density, and g gravitational acceleration.

The continuity equation is

$$-\frac{1}{r}\frac{\partial}{\partial r}(rv_r) + \frac{\partial v_z}{\partial z} = 0, \tag{5}$$

whereas the irrotationality condition is

$$\frac{\partial v_r}{\partial z} + \frac{\partial v_z}{\partial r} = 0. \tag{6}$$

The potential function satisfies the axisymmetric Laplace equation

$$\frac{1}{r}\frac{\partial}{\partial r}\left(r\frac{\partial \phi}{\partial r}\right) + \frac{\partial^2 \phi}{\partial z^2} = 0. \tag{7}$$

At the horizontal impermeable bed, the kinematic condition is [5, 10]

$$v_z(r, 0, t) = 0. \tag{8}$$

On the free boundary, the dynamic condition is [5, 10]

$$\phi(r, h, t) = h(r, t), \tag{9}$$

while the kinematic condition is

$$v_z(r, h, t) + v_r(r, h, t)\frac{\partial h}{\partial r} = \eta\frac{\partial h}{\partial t}, \tag{10}$$

where η is the effective porosity (specific yield) [10, 14].

At the outer radial boundary, $r = R$, the potential function is

$$\phi(R, z, t) = H, \qquad 0 \le z \le H. \tag{11}$$

On the well wall below the water level in the well, the potential function is

$$\phi(r_w, z, t) = h_w(t), \qquad 0 \le z \le h_w(t). \tag{12}$$

On the seepage face, the pressure is atmospheric and therefore

$$\phi(r_w, z, t) = z, \qquad h_w(t) \le z \le h(r_w, t). \tag{13}$$

For a prescribed pumping rate $Q_w(t)$, conservation of mass in the well gives [10, 14]

$$Q_w(t) = q(r_w, t) - \pi r_w^2 \frac{dh_w}{dt}, \tag{14}$$

where $q\,(r, t)$ is the flow rate

$$q(r, t) = 2\pi r \int_0^{h(r,t)} v_r(r, z, t)\, dz, \tag{15}$$

With the formulation adopted herein, the flow problem consists in finding the harmonic potential $\phi(r,z,t)$, the free-boundary position $h(r,t)$, and the water level in the well $h_w(t)$. The velocity and pressure fields are then obtained from Eqs. (2)–(4), while the seepage-face height $s_f(t)$ is obtained from Eq. (1).

3 Picard iteration

The axisymmetric velocity field $\boldsymbol{v}(r,z,t)$ is approximated by a Picard iteration that generalizes the procedure proposed in [18] for steady axisymmetric potential flow. The procedure involves the local flow rate and free-boundary elevation, without using the boundary conditions prescribed at the well.

Setting as a first approximation

$$v_r^{(1)} = \frac{F}{2\pi r}, \tag{16}$$

where $F(r,t)$ is defined as

$$F(r,t) = \frac{q(r,t)}{h(r,t)}, \tag{17}$$

and

$$v_z^{(1)} = 0, \tag{18}$$

the irrotationality condition is automatically satisfied. The solenoidality condition is verified if and only if the following first-order term is considered nil

$$\frac{\partial F}{\partial r} = 0. \tag{19}$$

Equation (19) defines the approximation order associated with Eqs. (16) and (18).

The second approximation of the velocity field can be deduced by setting

$$v_r^{(2)} = \frac{F}{2\pi r}, \tag{20}$$

$$v_z^{(2)} = f_2(r,z,t), \tag{21}$$

where $f_2(r,z,t)$ is a function unknown a priori. From the solenoidality condition, it follows that

$$\frac{\partial f_2}{\partial z} = \frac{1}{2\pi r}\frac{\partial F}{\partial r}. \tag{22}$$

Integration with respect to z gives

$$f_2 = \frac{z}{2\pi r}\frac{\partial F}{\partial r} + g_2(r,t). \tag{23}$$

Taking into account the kinematic condition at the horizontal impermeable bed, Eq. (8), it follows that $g_2(r,t) = 0$, and the second approximation of the vertical velocity component is given by

$$v_z^{(2)} = \frac{z}{2\pi r}\frac{\partial F}{\partial r}. \tag{24}$$

The velocity field given by Eqs. (20) and (24) is solenoidal. The velocity field itself is irrotational if and only if the following second-order term is considered nil

$$\frac{\partial}{\partial r}\left[\frac{1}{2\pi r}\frac{\partial F}{\partial r}\right] = 0. \tag{25}$$

Equation (25) defines the approximation order associated with Eqs. (20) and (24). For convenience, we set

$$A(r,t) = \frac{\partial}{\partial r}\left[\frac{1}{2\pi r}\frac{\partial F}{\partial r}\right]. \tag{26}$$

The third approximation of the velocity field can be deduced by setting

$$v_r^{(3)} = \frac{F}{2\pi r} + f_3(r,z,t), \tag{27}$$

$$v_z^{(3)} = \frac{z}{2\pi r}\frac{\partial F}{\partial r}. \tag{28}$$

From the irrotationality condition, it follows that

$$\frac{\partial f_3}{\partial z} = -zA. \tag{29}$$

Integration with respect to z gives

$$f_3 = -\frac{z^2}{2}A + g_3(r,t). \tag{30}$$

Taking into account the definition of the total radial flow rate given by Eq. (15), the function $g_3(r,t)$ is

$$g_3 = \frac{h^2}{6}A. \tag{31}$$

Consequently, the third approximation of the radial velocity component is given by

$$v_r^{(3)} = \frac{F}{2\pi r} + \left(\frac{h^2}{6} - \frac{z^2}{2}\right)A. \tag{32}$$

The corresponding vertical velocity component is

$$v_z^{(3)} = \frac{z}{2\pi r}\frac{\partial F}{\partial r}. \tag{33}$$

The velocity field given by Eqs. (32) and (33) is irrotational. Substitution into the continuity equation gives

$$-\frac{1}{r}\frac{\partial}{\partial r}\left(rv_r^{(3)}\right) + \frac{\partial v_z^{(3)}}{\partial z} = -\left(\frac{h^2}{6} - \frac{z^2}{2}\right)\frac{1}{r}\frac{\partial}{\partial r}(rA) - \frac{h}{3}\frac{\partial h}{\partial r}A. \tag{34}$$

Therefore, the solenoidality condition is verified by considering the following higher-order term nil

$$\frac{1}{r}\frac{\partial}{\partial r}(rA) = 0, \tag{35}$$

together with

$$A\frac{\partial h}{\partial r} = 0. \tag{36}$$

Equations (35) and (36) define the closure hypotheses associated with the third approximation of the velocity field.

By substituting Eqs. (17) and (26) into Eq. (32), the radial velocity component is finally written as

$$v_r = \frac{q}{2\pi r h} + \left(\frac{h^2}{6} - \frac{z^2}{2}\right)\frac{\partial}{\partial r}\left[\frac{1}{2\pi r}\frac{\partial}{\partial r}\left(\frac{q}{h}\right)\right]. \tag{37}$$

The vertical velocity component is

$$v_z = \frac{z}{2\pi r}\frac{\partial}{\partial r}\left(\frac{q}{h}\right). \tag{38}$$

The approximation given by Eqs. (37) and (38) contains radial derivatives up to the second order and does not depend on the particular conditions imposed at the radial boundaries. The equivalence between the third Picard approximation and the corresponding truncation of the long-wave expansion is shown in Appendix B. Higher-order terms generated by further Picard iterations are neglected according to the closure hypotheses given by Eqs. (35) and (36). For steady flow, the flow rate is independent of r, and the above procedure reduces to the Picard iteration and closure hypotheses given in [18].

4 One-dimensional model

4.1 Model equations

By using the approximate vertical velocity component given by Eq. (38), together with Darcy's law, Eq. (3), and the dynamic condition at the free boundary, Eq. (9), the potential function is written as

$$\phi(r, z, t) = h + \frac{h^2 - z^2}{4\pi k r}\frac{\partial}{\partial r}\left(\frac{q}{h}\right). \tag{39}$$

By substituting Eq. (39) into the radial component of Darcy's law, Eq. (2), and taking into account the definition of the flow rate given by Eq. (15), we obtain

$$\frac{q}{2\pi k r} = \frac{\partial}{\partial r}\left[\frac{h^2}{2} + \frac{h^3}{6\pi k r}\frac{\partial}{\partial r}\left(\frac{q}{h}\right)\right]. \tag{40}$$

Equation (40) represents the one-dimensional momentum equation.

The one-dimensional continuity equation can be deduced as follows. By integrating Eq. (5) between $z = 0$ and $z = h(r, t)$, and taking into account Eq. (8) and the definition of the flow rate, Eq. (15), we obtain

$$\frac{1}{2\pi}\frac{\partial q}{\partial r} = r\left[v_z(r,h,t) + v_r(r,h,t)\frac{\partial h}{\partial r}\right]. \tag{41}$$

By using the kinematic condition at the free boundary, Eq. (10), Eq. (41) gives

$$\frac{\partial q}{\partial r} = 2\pi r\eta\frac{\partial h}{\partial t}. \tag{42}$$

Equation (42) represents the one-dimensional continuity equation.

The one-dimensional model is given by the system of Eqs. (40) and (42), whose unknowns are $h(r,t)$ and $q(r,t)$. These equations are obtained without using the boundary conditions at the well and at the outer radial boundary. Their solution requires appropriate initial and boundary conditions for the flow configuration under consideration.

4.2 Application to a fully penetrating well

For the problem defined in Section 2, the system is completed by the initial and boundary conditions, together with the well mass-balance equation, Eq. (14).

The system is further completed by the axisymmetric Cauchy integral relation derived in Appendix A. Using the boundary conditions prescribed for the well problem, this relation is written as

$$\frac{h_w^2}{2} = \frac{H^2}{2} - \int_{r_w}^{R}\frac{q(r,t)}{2\pi kr}\,dr. \tag{43}$$

The seepage-face height is obtained from Eq. (1).

We stress that, for steady flow, Eq. (40) reduces to the axisymmetric model derived in [18, 19], for which the free boundary is given by

$$\frac{h^2}{2} = \frac{H^2}{2} - \frac{1}{2\pi}\frac{q}{k}\ln\left(\frac{R}{r}\right) + \frac{1}{4\pi}\frac{q}{k}e^u\left[E_1(u) - E_1(u_+)\right]. \tag{44}$$

where $q = Q_w$ is the constant steady flow rate. From Eq. (43), the steady flow rate is related to the water levels by

$$q = Q_w = \frac{\pi k\left(H^2 - h_w^2\right)}{\ln\left(R/r_w\right)}. \tag{45}$$

Moreover,

$$u = \frac{3\pi r^2}{q/k}, \tag{46}$$

$$u_+ = \frac{3\pi R^2}{q/k}. \tag{47}$$

The function E_1 is the exponential integral defined as

$$E_1(u) = \int_u^{\infty}\frac{e^{-t}}{t}\,dt. \tag{48}$$

4.3 Numerical solution and validation

The present model is validated against the pumping-well problem considered by Lennon et al. [10]. Following [10], dimensionless variables are introduced by using the well radius r_w as characteristic length, $\eta r_w/k$ as characteristic time, and kr_w^2 as characteristic flow rate. Accordingly,

$$\begin{aligned} \tilde{r} &= \frac{r}{r_w}, \quad \tilde{h} = \frac{h}{r_w}, \quad \tilde{h}_w = \frac{h_w}{r_w}, \quad \tilde{H} = \frac{H}{r_w}, \\ \tilde{R} &= \frac{R}{r_w}, \quad \tilde{t} = \frac{kt}{\eta r_w}, \quad \tilde{q} = \frac{q}{kr_w^2}, \quad \tilde{Q}_w = \frac{Q_w}{kr_w^2}. \end{aligned} \tag{49}$$

The dimensionless seepage-face height is defined as

$$\tilde{s}_f = \frac{s_f}{r_w}. \tag{50}$$

In dimensionless form, Eqs. (40) and (42) become

$$\frac{\tilde{q}}{2\pi\tilde{r}} = \frac{\partial}{\partial\tilde{r}}\left[\frac{\tilde{h}^2}{2} + \frac{\tilde{h}^3}{6\pi\tilde{r}}\frac{\partial}{\partial\tilde{r}}\left(\frac{\tilde{q}}{\tilde{h}}\right)\right], \tag{51}$$

and

$$\frac{\partial\tilde{q}}{\partial\tilde{r}} = 2\pi\tilde{r}\frac{\partial\tilde{h}}{\partial\tilde{t}}. \tag{52}$$

The dimensionless well mass-balance equation is

$$\tilde{Q}_w = \tilde{q}(1,\tilde{t}) - \frac{\pi}{\eta}\frac{d\tilde{h}_w}{d\tilde{t}}, \tag{53}$$

while Eq. (43) becomes

$$\frac{\tilde{h}_w^2}{2} = \frac{\tilde{H}^2}{2} - \int_1^{\tilde{R}} \frac{\tilde{q}(\tilde{r},\tilde{t})}{2\pi\tilde{r}}\, d\tilde{r}. \tag{54}$$

The initial free boundary is horizontal and is given by

$$\tilde{h}(\tilde{r},0) = \tilde{H}, \tag{55}$$

while the initial water level in the well is

$$\tilde{h}_w(0) = \tilde{H}. \tag{56}$$

At the outer radial boundary,

$$\tilde{h}(\tilde{R},\tilde{t}) = \tilde{H}. \tag{57}$$

The prescribed potential condition, Eq. (11), together with Eq. (39) and Eq. (57), gives

$$\left.\frac{\partial}{\partial \tilde{r}}\left(\frac{\tilde{q}}{\tilde{h}}\right)\right|_{\tilde{r}=\tilde{R}} = 0. \tag{58}$$

The interval $1 \leq \tilde{r} \leq \tilde{R}$ is discretized by means of a non-uniform radial grid, with the nodes logarithmically spaced in order to increase the spatial resolution near the well. Equation (51) is written in terms of $\tilde{q}/\tilde{h}$ and is discretized in conservative form by means of second-order finite differences on the non-uniform grid. For given values of the free-boundary position $\tilde{h}$ and the water level in the well $\tilde{h}_w$, the flow rate $\tilde{q}$ is obtained by solving the resulting linear algebraic system. The system is completed by the outer-boundary condition, Eq. (58), and by the Cauchy integral relation, Eq. (54). The integral in Eq. (54) is evaluated by the trapezoidal rule.

Once the flow-rate distribution is determined, Eq. (52) provides the time derivative of the free-boundary position, while Eq. (53) provides the time derivative of the water level in the well. The resulting system is integrated with an implicit variable-order BDF method with adaptive time stepping. The calculations reported in the next section are performed with $N_r = 161$ radial nodes and with a maximum dimensionless time step equal to 0.2. Relative and absolute integration tolerances are 2×10^{-7} and 10^{-9}, respectively. Grid independence was checked by repeating the calculations with $N_r = 41$, 81, and 161. The maximum difference between the free-boundary profiles obtained with 81 and 161 nodes was less than 8×10^{-3}.

4.4 Numerical results

The test case is characterized by

$$\tilde{R} = 16, \tag{59}$$

$$\tilde{H} = 10, \tag{60}$$

$$\eta = 0.30, \tag{61}$$

and by the constant pumping rate

$$\tilde{Q}_w = 106.23. \tag{62}$$

The constant pumping rate is applied at $\tilde{t} = 0^+$. The value $\eta = 0.30$ corresponds to the specific yield adopted by Neuman and Witherspoon [1] for the unsteady well problem considered by Lennon et al. [10]. The value of $\tilde{Q}_w$ corresponds to the steady-state Dupuit flow rate associated with a dimensionless water level in the well equal to $\tilde{h}_w = 2.5$ [10].

Figure 2 shows the free-boundary profiles obtained at selected dimensionless times. The present model results are compared with the BIEM results reported in [10]. The comparison is performed at $\tilde{t} = 1.4$, 3.5, 9.1, 23.6, and 60. At $\tilde{t} = 60$, the flow is approximately at steady state. The BIEM reference data were digitized from the free-boundary profiles reported by Lennon et al. [10].

For a quantitative comparison, the maximum normalized difference is defined as

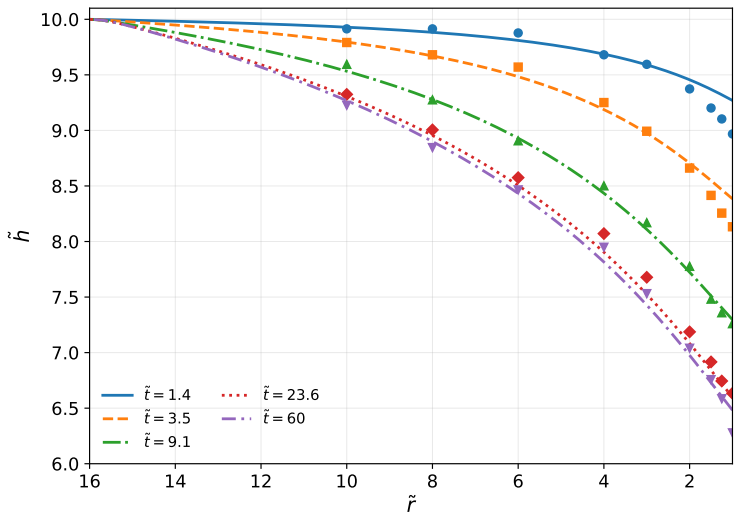


Fig. 2 Dimensionless free-boundary profiles at selected times. Lines: present model; symbols: BIEM results digitized from [10].

$$\delta_\infty(\tilde{t}) = \frac{1}{\tilde{H}} \max_j \left| \tilde{h}_{\mathrm{model}}(\tilde{r}_j, \tilde{t}) - \tilde{h}_{\mathrm{BIEM}}(\tilde{r}_j, \tilde{t}) \right|, \tag{63}$$

while the root-mean-square normalized difference is

$$\delta_{\mathrm{RMS}}(\tilde{t}) = \frac{1}{\tilde{H}} \left[\frac{1}{N} \sum_{j=1}^{N} \left(\tilde{h}_{\mathrm{model}}(\tilde{r}_j, \tilde{t}) - \tilde{h}_{\mathrm{BIEM}}(\tilde{r}_j, \tilde{t}) \right)^2 \right]^{1/2}. \tag{64}$$

where N is the number of digitized BIEM data points and $\tilde{r}_j$ denotes the corresponding radial position. To assess the differences near the well, a local root-mean-square normalized difference $\delta_{\mathrm{RMS},w}$ is also evaluated in the region $1 \le \tilde{r} \le 2$. The obtained values are reported in Table 1. The largest local RMS difference occurs at $\tilde{t} = 1.4$ and is approximately 2.0% of the initial height.

The BIEM reference profile used at $\tilde{t} = 60$ corresponds to the approximately steady-state data reported for $\tilde{t} > 50$ in [10].

The obtained results show satisfactory agreement over the flow domain. The maximum normalized difference does not exceed 2.9%, while the root-mean-square difference remains below 1.4%. The largest local differences occur in the inner part of the flow domain, where the free-boundary curvature and vertical-flow effects are more pronounced. The model reproduces the progressive evolution toward the steady-state configuration.

Figure 3 shows the time evolution of the dimensionless water level in the well. The present model reproduces the initial drawdown and the subsequent approach to the steady-state value $\tilde{h}_w = 2.5$. The BIEM values shown in the figure were digitized from the water-level history reported by Lennon et al. [10]. In the BIEM calculations reported therein, the steady-state condition is approximately reached for dimensionless

Table 1 Normalized differences between the present model and the BIEM free-boundary data digitized from [10]. All differences are normalized by the initial water level $\tilde{H}$. The near-well RMS difference is evaluated over $1 \leq \tilde{r} \leq 2$.

$\tilde{t}$	δ_∞	δ_{RMS}	$\delta_{\mathrm{RMS},w}$
1.4	0.0288	0.0137	0.0202
3.5	0.0231	0.0114	0.0162
9.1	0.0062	0.0049	0.0051
23.6	0.0178	0.0095	0.0061
60	0.0203	0.0092	0.0106

times of the order of $\tilde{t} = 60$. At $\tilde{t} = 60$, the present model gives $\tilde{h}_w = 2.501$. Since the pumping rate was determined from Eq. (45) by imposing $\tilde{h}_w = 2.5$ at steady state, this result represents a consistency check. The comparison with the BIEM data provides an assessment of the transient evolution.

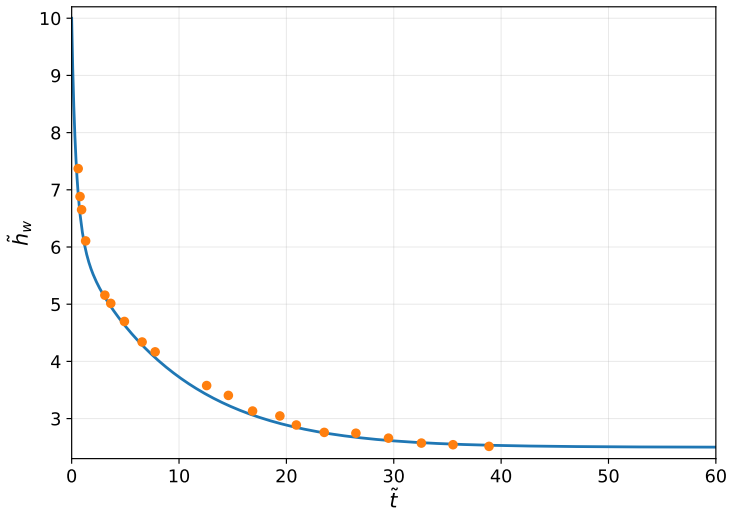


Fig. 3 Time evolution of the dimensionless water level in the well. Solid line: present model; symbols: BIEM results digitized from [10].

Figure 4 shows the seepage-face time evolution in dimensionless form. Starting from the initial condition $\tilde{s}_f(0) = 0$, the seepage-face height increases rapidly, reaches a local maximum, then slightly decreases to a local minimum, and subsequently increases toward the steady-state value.

The non-monotonic behavior can be interpreted as follows. From Eqs. (1) and (50), the dimensionless seepage-face height can be written as $\tilde{s}_f = \tilde{h}(1,\tilde{t}) - \tilde{h}_w(\tilde{t})$. Differentiating with respect to time and using Eqs. (52) and (53), we obtain

$$\frac{d\tilde{s}_f}{d\tilde{t}} = \frac{1}{2\pi}\frac{\partial \tilde{q}}{\partial \tilde{r}}\bigg|_{\tilde{r}=1} + \frac{\eta}{\pi}\left[\tilde{Q}_w - \tilde{q}(1,\tilde{t})\right]. \tag{65}$$

According to Eq. (52), the first term on the right-hand side of Eq. (65) is equal to $\partial\tilde{h}/\partial\tilde{t}$ at $\tilde{r} = 1$, and therefore represents the time variation of the free-boundary elevation at the well. According to Eq. (53), the second term is equal to $-d\tilde{h}_w/d\tilde{t}$. At $\tilde{t} = 0^+$, the first term is zero and Eq. (65) gives $d\tilde{s}_f/d\tilde{t} = \eta\tilde{Q}_w/\pi = 10.14$. Thus, immediately after pumping starts, the seepage-face height increases because the water level in the well decreases while the free boundary remains initially at rest.

As the flow develops, the free-boundary elevation at the well also decreases. When its rate of decrease becomes larger than that of the water level in the well, the seepage-face height decreases. At later times, the rate of decrease of the free-boundary elevation becomes smaller than that of the water level in the well, and the seepage-face height increases again toward the steady-state value. The local maximum and minimum shown in Fig. 4 correspond to the instants at which the two contributions in Eq. (65) balance. At steady state, $\partial\tilde{q}/\partial\tilde{r} = 0$ and $\tilde{q}(1) = \tilde{Q}_w$, and therefore $d\tilde{s}_f/d\tilde{t} = 0$.

For comparison, the BIEM seepage-face values were reconstructed as the difference between the free-boundary elevation at the well and the water level in the well, both digitized from the results reported by Lennon et al. [10]. The reconstructed values are affected by the graphical resolution of the published data. Consequently, the comparison is mainly qualitative.

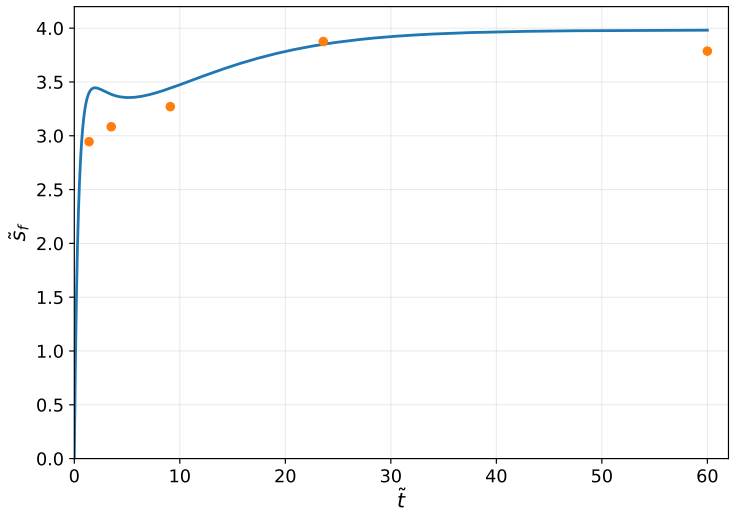


Fig. 4 Time evolution of the dimensionless seepage-face height. Solid line: present model; symbols: values reconstructed from the digitized BIEM results of [10].

The range of validity of the approximation can also be examined by using the criterion adopted in [18]. This criterion requires the radial velocity component to be non-negative at the free boundary, i.e.,

$$v_r(r, h, t) \geq 0. \tag{66}$$

From Eq. (39) and the radial component of Darcy's law, Eq. (2), we obtain

$$\frac{v_r}{k}\bigg|_{z=h} = \frac{\partial h}{\partial r}\left[1 + \frac{h}{2\pi k r}\frac{\partial}{\partial r}\left(\frac{q}{h}\right)\right]. \tag{67}$$

In dimensionless form, the corresponding condition is

$$\frac{\partial \tilde{h}}{\partial \tilde{r}}\left[1 + \frac{\tilde{h}}{2\pi\tilde{r}}\frac{\partial}{\partial \tilde{r}}\left(\frac{\tilde{q}}{\tilde{h}}\right)\right] \geq 0. \tag{68}$$

For steady flow, this condition reduces to the validity criterion derived in [18]. For the test case considered herein, the condition is satisfied during the initial stage of the flow, while at later times it is locally violated in the region close to the well. At approximately steady-state conditions, the region of violation is limited to $\tilde{r} \lesssim 1.28$. This result is consistent with the larger differences observed in the inner part of the flow domain, where the free-boundary curvature and vertical-flow effects are more pronounced. Since the seepage-face height is evaluated at $\tilde{r} = 1$, this local violation may affect the accuracy of the results shown in Fig. 4.

The comparison shows that the present model reproduces the main features of the unsteady axisymmetric flow in the reference well problem, including the free-boundary evolution, the water-level drawdown in the well, and the seepage-face development.

For the sake of completeness, the results obtained with the present model are also compared with those given by the classical Dupuit–Forchheimer approximation. The latter is obtained by neglecting the vertical-flow correction in Eq. (51). The Dupuit–Forchheimer equation reads as

$$\frac{\tilde{q}}{2\pi\tilde{r}} = \frac{\partial}{\partial \tilde{r}}\left(\frac{\tilde{h}^2}{2}\right). \tag{69}$$

The same initial conditions, pumping rate, and well-storage equation are considered. Figure 5 shows the free-boundary profiles obtained with the two models at $\tilde{t} = 3.5$ and $\tilde{t} = 60$. Since the Dupuit–Forchheimer approximation does not account for the seepage face (under the Dupuit-Forchheimer approximation, we get $\tilde{h}(1, \tilde{t}) = \tilde{h}_w(\tilde{t})$), the differences are more pronounced in the region close to the well and decrease with increasing radial distance.

4.5 Comparison with VarSatFlow

The present model is also compared with numerical results obtained using VarSatFlow [2]. VarSatFlow describes variably saturated flow by coupling gravity-driven flow in unsaturated regions with Darcy flow in saturated regions. The model determines the water saturation S_w, defined as the fraction of pore volume occupied by water. The

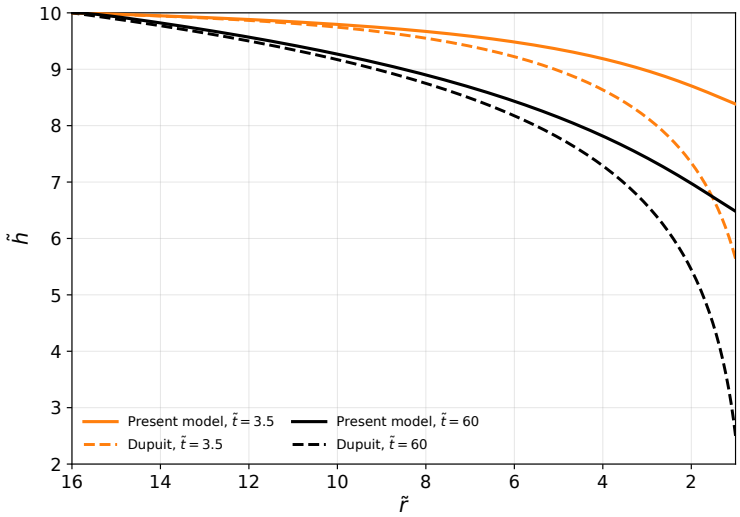


Fig. 5 Dimensionless free-boundary profiles at $\tilde{t} = 3.5$ and $\tilde{t} = 60$. Solid lines: present model; dashed lines: Dupuit–Forchheimer approximation.

saturated–unsaturated interface is obtained from the saturation field without explicitly tracking a free boundary. In the present comparison, the free-boundary position is estimated using the contour $S_w = 0.999$.

The same flow configuration is considered, with $\tilde{R} = 16$, $\tilde{H} = 10$, and $\eta = 0.30$. The water level in the well is suddenly reduced to $\tilde{h}_w = 2.5$ at $\tilde{t} = 0^+$ and then kept constant.

The one-dimensional model equations are given by Eqs. (51) and (52), together with the Cauchy integral relation (54). The well mass-balance equation (53) is replaced by the prescribed water level in the well. The initial free boundary is horizontal, with $\tilde{h}(\tilde{r}, 0) = 10$. The equations are integrated numerically using the radial discretization and the implicit time-integration method described in Section 4.3. The VarSatFlow formulation and numerical setup are described in Appendix C.

Figure 6 shows the free-boundary profiles obtained with the present model and the water-saturation fields computed with VarSatFlow at selected dimensionless times. In the VarSatFlow simulations, drainage develops close to the well and progressively extends toward the outer boundary. The saturated height near the well decreases and approaches an approximately stationary value.

For a quantitative comparison, the saturated-contour height $\tilde{h}_{0.999}$ obtained with VarSatFlow is compared with the free-boundary elevation predicted by the present model. The comparison is performed at $\tilde{r} = 1.05$, the center of the first radial cell of the VarSatFlow grid. The relative difference is defined as

$$\delta_{\mathrm{rel}}(\tilde{t}) = \frac{\left|\tilde{h}_{\mathrm{model}}(1.05, \tilde{t}) - \tilde{h}_{0.999}(1.05, \tilde{t})\right|}{\tilde{h}_{0.999}(1.05, \tilde{t})}. \tag{70}$$

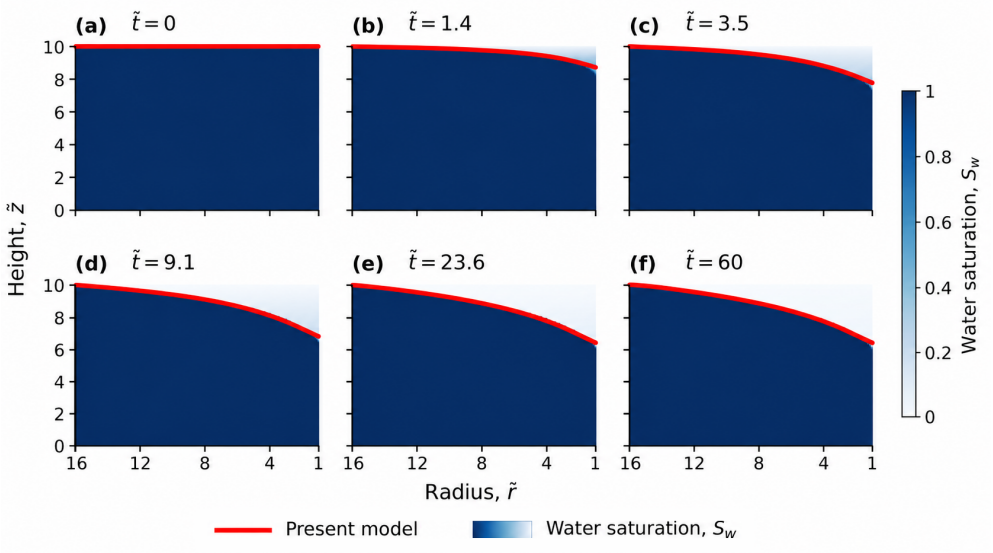


Fig. 6 Comparison between the present model and VarSatFlow for the prescribed well-water level $\tilde{h}_w = 2.5$ at selected dimensionless times. Red lines: present model; blue shading: VarSatFlow water saturation S_w.

Table 2 Comparison between the free-boundary elevation predicted by the present model and the saturated-contour height obtained with VarSatFlow at $\tilde{r} = 1.05$.

$\tilde{t}$	$\tilde{h}_{\mathrm{model}}$	$\tilde{h}_{0.999}$	δ_{rel}
0	10.000	10.000	0.00
1.4	8.753	8.151	0.0739
3.5	7.812	7.250	0.0775
9.1	6.889	6.450	0.0681
23.6	6.526	6.051	0.0785
60	6.501	6.050	0.0745

The present model predicts a higher free-boundary elevation near the well than VarSatFlow. As shown in Table 2, the relative percentage difference ranges from approximately 6.8% to 7.9%. It should be noted that the present model describes a sharp free boundary, whereas the saturated-contour height in VarSatFlow depends on the adopted saturation threshold.

5 Conclusion

In this paper, one-dimensional model equations for unsteady axisymmetric free-boundary potential flow in porous media have been derived. A Picard iteration has

been employed to obtain successive approximations of the irrotational and solenoidal velocity field. The third approximation has been used to derive a one-dimensional momentum equation accounting for vertical-flow effects, while the one-dimensional continuity equation has been obtained directly from mass conservation. These equations do not depend on the particular boundary conditions adopted for the pumping-well problem.

The present formulation extends the steady axisymmetric Picard model of [18, 19] to unsteady flow. The axisymmetric counterpart of the Cauchy integral relation employed in [5] has also been derived. For the fully penetrating well, this relation and the well mass-balance equation complete the one-dimensional model. Under steady-flow conditions, the formulation reduces to the previously derived steady axisymmetric model [18, 19].

The model has been tested against the unsteady pumping-well problem considered by Lennon et al. [10]. The numerical results show satisfactory agreement with the BIEM results for the free-boundary evolution, the water level in the well, and the seepage-face development. For the free-boundary profiles, the maximum normalized difference does not exceed 2.9%, while the root-mean-square normalized difference remains below 1.4%. The largest differences occur near the well.

The model has also been compared with VarSatFlow simulations [2] under prescribed well-water-level conditions. The present model predicts a higher free-boundary elevation near the well than the saturated-contour height obtained with VarSatFlow. The relative percentage difference at $\tilde{r} = 1.05$ ranges from 6.8% to 7.9% at selected times.

Declarations

Data availability

The numerical data supporting the findings of this study, including the computed free-boundary profiles, well-water levels, and seepage-face elevations, are available from the corresponding author upon reasonable request.

Funding

The authors received no funding for this research.

Competing interests

The authors declare no competing interests.

Author contributions

All authors contributed equally to this work. All authors have read and approved the final manuscript.

Ethics approval

Not applicable.

Consent to participate

Not applicable.

Consent for publication

Not applicable.

Appendix A Axisymmetric Cauchy integral relation

For the axisymmetric flow problem, the stream function $\psi(r, z, t)$ associated with the solenoidal vector field is given by

$$\frac{\partial \psi}{\partial z} = r v_r, \tag{A1}$$

$$\frac{\partial \psi}{\partial r} = r v_z. \tag{A2}$$

According to Eqs. (2) and (3), and using Eq. (A1), the axisymmetric counterparts of the Cauchy–Riemann relations are written as

$$\frac{\partial \phi}{\partial r} = \frac{1}{kr}\frac{\partial \psi}{\partial z}, \tag{A3}$$

and

$$\frac{\partial \phi}{\partial z} = -\frac{1}{kr}\frac{\partial \psi}{\partial r}. \tag{A4}$$

Over any simple closed curve C^+ contained in the flow domain, Green's theorem [30] gives

$$\oint_{C^+} \left(\phi\, dz + \frac{\psi}{kr}\, dr\right) = \iint_D \left[\frac{\partial \phi}{\partial r} - \frac{\partial}{\partial z}\left(\frac{\psi}{kr}\right)\right] dr\, dz, \tag{A5}$$

where D is the region enclosed by C^+. Since r is independent of z, Eq. (A3) gives

$$\frac{\partial \phi}{\partial r} - \frac{\partial}{\partial z}\left(\frac{\psi}{kr}\right) = 0. \tag{A6}$$

Therefore,

$$\oint_{C^+} \left(\phi\, dz + \frac{\psi}{kr}\, dr\right) = 0. \tag{A7}$$

Equation (A7) is the axisymmetric counterpart of the Cauchy integral relation employed for two-dimensional free-boundary flows in porous media [5].

Identifying C^+ with the boundary of the flow domain, taken positive in the counterclockwise direction, Eq. (A7) is evaluated by using the prescribed boundary conditions. Without loss of generality, at the horizontal impermeable bed we take $\psi = 0$; on the free boundary, taking into account Eq. (15),

$$\psi = r \int_0^h v_r \, dz = \frac{q(r,t)}{2\pi}. \tag{A8}$$

At the outer radial boundary, Eq. (11) gives $\phi = H$, whereas on the free boundary, Eq. (9) gives

$$\phi = h. \tag{A9}$$

Along the well wall, below the water level in the well, Eq. (12) gives

$$\phi(r_w, z, t) = h_w(t), \qquad 0 \le z \le h_w(t). \tag{A10}$$

On the seepage face, Eq. (13) gives

$$\phi(r_w, z, t) = z, \qquad h_w(t) \le z \le h(r_w, t). \tag{A11}$$

The contributions along the different portions of the boundary therefore give

$$H^2 + \int_R^{r_w} \left[h \frac{\partial h}{\partial r} + \frac{q(r,t)}{2\pi k r} \right] dr + \int_{h(r_w,t)}^{h_w(t)} z \, dz + \int_{h_w(t)}^{0} h_w(t) \, dz = 0. \tag{A12}$$

After integration and algebra, Eq. (A12) becomes

$$\frac{h_w^2}{2} = \frac{H^2}{2} - \int_{r_w}^{R} \frac{q(r,t)}{2\pi k r} \, dr. \tag{A13}$$

Equation (A13) is the axisymmetric Cauchy integral relation employed for the well problem in Section 4. Its integral form, Eq. (A7), follows from the governing equations, while Eq. (A13) also uses the prescribed boundary conditions. Neither relation depends on the approximation introduced by the Picard iteration.

Appendix B Relation between the Picard iteration and the long-wave approximation

Long-wave approximations for free-surface flow in porous media have been considered in [31, 32]. We show that the third approximation of the velocity field obtained by means of the Picard iteration coincides with the corresponding long-wave approximation. Let L and H_0 be characteristic radial and vertical lengths, respectively, and set

$$\varepsilon = \frac{H_0}{L}, \qquad \varepsilon \ll 1. \tag{B14}$$

We introduce the dimensionless coordinates $x = r/L$ and $\zeta = z/H_0$, and write

$$h(r,t) = H_0 b(x,t), \tag{B15}$$

$$\frac{F(r,t)}{2\pi r} = U f(x,t). \tag{B16}$$

where U is a characteristic radial velocity. Time is treated as a parameter in the following derivation. We assume that b, f, and their dimensionless radial derivatives remain of order unity in the region considered.

According to the continuity equation, the characteristic vertical velocity is εU. Setting

$$v_r = Uu(x, \zeta, t), \tag{B17}$$

$$v_z = \varepsilon U w(x, \zeta, t). \tag{B18}$$

Eqs. (5) and (6) become

$$-\frac{1}{x}\frac{\partial}{\partial x}(xu) + \frac{\partial w}{\partial \zeta} = 0, \tag{B19}$$

and

$$\frac{\partial u}{\partial \zeta} + \varepsilon^2 \frac{\partial w}{\partial x} = 0. \tag{B20}$$

Equation (B20) shows that the vertical variation of the radial velocity is a second-order effect.

We consider the expansions

$$u = u_0 + \varepsilon^2 u_2 + O(\varepsilon^4), \tag{B21}$$

$$w = w_0 + \varepsilon^2 w_2 + O(\varepsilon^4). \tag{B22}$$

At leading order, Eq. (B20) gives $\partial u_0/\partial \zeta = 0$. From the definition of F, Eq. (17), and Eq. (B16), it follows that $u_0 = f$. Substitution into Eq. (B19), together with the impermeable-bed condition, gives

$$w_0 = \zeta B, \tag{B23}$$

$$B(x, t) = \frac{1}{x}\frac{\partial}{\partial x}(xf). \tag{B24}$$

At order ε^2, Eq. (B20) gives

$$\frac{\partial u_2}{\partial \zeta} = -\zeta \frac{\partial B}{\partial x}. \tag{B25}$$

The definition of the flow rate implies that the depth average of u_2 vanishes. Integration of Eq. (B25) therefore gives

$$u_2 = \left(\frac{b^2}{6} - \frac{\zeta^2}{2}\right)\frac{\partial B}{\partial x}. \tag{B26}$$

Consequently, retaining u_0, u_2, and w_0, the velocity field is

$$v_r = U\left[f + \varepsilon^2 \left(\frac{b^2}{6} - \frac{\zeta^2}{2}\right)\frac{\partial B}{\partial x}\right], \tag{B27}$$

$$v_z = \varepsilon U \zeta B. \tag{B28}$$

Returning to dimensional variables, the above expressions give Eqs. (37) and (38). Therefore, the third Picard approximation coincides with the long-wave approximation at the order considered.

The continuity equation provides the order of the neglected terms. Substituting Eqs. (B27) and (B28) into Eq. (B19), we obtain

$$\begin{aligned} -\frac{1}{x}\frac{\partial}{\partial x}(xu) + \frac{\partial w}{\partial \zeta} = -\varepsilon^2 \Bigg[\left(\frac{b^2}{6} - \frac{\zeta^2}{2}\right) \frac{1}{x}\frac{\partial}{\partial x}\left(x\frac{\partial B}{\partial x}\right) \\ + \frac{b}{3}\frac{\partial b}{\partial x}\frac{\partial B}{\partial x}\Bigg]. \end{aligned} \tag{B29}$$

Equation (B29) is the dimensionless form of Eq. (34). In the long-wave expansion, this residual is balanced by the term $\varepsilon^2 w_2$ in Eq. (B22). Taking into account the impermeable-bed condition, the corresponding correction is

$$\begin{aligned} w_2 = \left(\frac{b^2\zeta}{6} - \frac{\zeta^3}{6}\right) \frac{1}{x}\frac{\partial}{\partial x}\left(x\frac{\partial B}{\partial x}\right) \\ + \frac{b\zeta}{3}\frac{\partial b}{\partial x}\frac{\partial B}{\partial x}. \end{aligned} \tag{B30}$$

The terms neglected according to the closure hypotheses, Eqs. (35) and (36), correspond to higher-order contributions in the long-wave expansion. In particular, the correction to the vertical velocity is of order $\varepsilon^3 U$. Therefore, the third Picard approximation is consistent with the long-wave approximation at the order considered.

The above result holds under the assumption of small depth-to-length ratio and bounded dimensionless radial derivatives. These conditions may not be satisfied in regions characterized by rapid radial variations of the flow, as may occur near the well. The result does not establish uniform accuracy of the model throughout the flow domain.

Appendix C VarSatFlow model and numerical setup

C.1 Model and numerical method

We simulate variably saturated flow using VarSatFlow [2], which couples gravity-driven transport in unsaturated regions to an elliptic Darcy problem in saturated regions. The formulation assumes incompressible water, a rigid porous matrix, negligible capillary forces, and atmospheric gas pressure. Saturation evolves through water conservation, while the saturated hydraulic head is determined from incompressibility. The saturated—unsaturated interface emerges from the saturation field without

explicit interface tracking. In axisymmetric coordinates, water conservation is

$$\eta \frac{\partial S_w}{\partial t} - \frac{1}{r}\frac{\partial (r v_r)}{\partial r} + \frac{\partial v_z}{\partial z} = 0, \tag{C31}$$

where z increases upward, S_w is water saturation, η is the effective porosity, and v_r and v_z are the Darcy velocity components, positive toward the well and upward, respectively. For the constitutive law used here,

$$\begin{aligned} v_r &= \begin{cases} 0, & S_w < 1, \\ k\dfrac{\partial \phi}{\partial r}, & S_w = 1, \end{cases} \\ v_z &= \begin{cases} -kS_w^2, & S_w < 1, \\ -k\dfrac{\partial \phi}{\partial z}, & S_w = 1, \end{cases} \end{aligned} \tag{C32}$$

where k is the saturated hydraulic conductivity and ϕ is the hydraulic potential defined in the main text. The saturated problem therefore satisfies $\nabla \cdot (k \nabla \phi) = 0$. The numerical method places saturation and potential at cell centers and fluxes at cell faces, with upwind unsaturated transport and explicit Euler updates [2]. Here, the discrete divergence includes cylindrical geometry, and the time step accounts for available pore space and drainable water.

C.2 Initial and boundary conditions

The domain represents a homogeneous, isotropic aquifer with $1 \le \tilde{r} \le 16$ and $0 \le \tilde{z} \le 10$, where lengths are normalized by the well radius r_w. The effective porosity is $\eta = 0.30$, residual water and gas saturations are zero, and the normalized saturated hydraulic conductivity is unity. The relative permeability is $k_{rw} = S_w^2$. A uniform grid of 150×100 cells gives $\Delta\tilde{r} = \Delta\tilde{z} = 0.1$. Initially, $S_w = 1$ throughout the domain and the horizontal water table is at $\tilde{h} = 10$.

The outer reservoir maintains hydraulic potential $\tilde{\phi} = 10$. At the inner boundary, the well water level is fixed at $\tilde{h}_w = 2.5$: the submerged boundary remains saturated with hydraulic potential $\tilde{\phi} = 2.5$, while the exposed boundary has atmospheric pressure and permits discharge toward the well, $v_r \ge 0$. Both horizontal boundaries have zero water flux, representing no surface recharge and an impermeable base. Well storage is omitted, and the well discharge responds to the prescribed reservoir heads. This is a fixed-head drainage problem.

We report time as $\tilde{t} = kt/(\eta r_w)$, so that $t_{\mathrm{code}} = 0.30\tilde{t}$. The archive contains 601 states over $0 \le t_{\mathrm{code}} \le 20$. Profiles are examined at $\tilde{t} = 0$, 1.4, 3.5, 9.1, 23.6, and 60. Where necessary, saturation is interpolated between saved states before extracting a contour. The saturated region is identified by $S_w \ge 0.999$. Its upper boundary defines a contour-based height $\tilde{h}_{0.999}$. The sampling radius $\tilde{r} = 1.05$ is the center of the first radial cell.

C.3 Simulation results

Drainage develops most strongly near the well and extends outward while the outer reservoir maintains the saturated boundary. The well-adjacent contour has nearly stabilized by $\tilde{t} = 23.6$. The saturation fields and the comparison with the one-dimensional model are presented in Section 4.5.

References

[1] Neuman, S.P., Witherspoon, P.A.: Analysis of nonsteady flow with a free surface using the finite element method. Water Resources Research **7**(3), 611–623 (1971) https://doi.org/10.1029/WR007i003p00611

[2] Shadab, M.A., Hesse, M.A.: A hyperbolic–elliptic pde model and conservative numerical method for gravity-dominated variably-saturated groundwater flow. Advances in Water Resources **190**, 104736 (2024) https://doi.org/10.1016/j.advwatres.2024.104736

[3] Knight, J.H.: Improving the Dupuit–Forchheimer groundwater free surface approximation. Advances in Water Resources **28**(10), 1048–1056 (2005) https://doi.org/10.1016/j.advwatres.2005.04.014

[4] Castro-Orgaz, O.: Steady free-surface flow in porous media: generalized Dupuit–Fawer equations. Journal of Hydraulic Research **49**(1), 55–63 (2011) https://doi.org/10.1080/00221686.2010.526758

[5] Di Nucci, C.: Unsteady free surface flow in porous media: One-dimensional model equations including vertical effects and seepage face. Comptes Rendus Mecanique **346**(5), 366–383 (2018) https://doi.org/10.1016/j.crme.2018.03.003

[6] Chenaf, D., Chapuis, R.P.: Seepage face height, water table position, and well efficiency at steady state. Ground Water **45**(2), 168–177 (2007) https://doi.org/10.1111/j.1745-6584.2006.00277.x

[7] Liggett, J.A.: Location of free surface in porous media. Journal of the Hydraulics Division, ASCE **103**(HY4), 353–365 (1977) https://doi.org/10.1061/JYCEAJ.0004730

[8] Liu, P.L.-F., Liggett, J.A.: Boundary solutions to two problems in porous media. Journal of the Hydraulics Division, ASCE **105**(HY3), 171–183 (1979) https://doi.org/10.1061/JYCEAJ.0005156

[9] Lennon, G.P., Liu, P.L.-F., Liggett, J.A.: Boundary integral equation solution to axisymmetric potential flows: 1. basic formulation. Water Resources Research **15**(5), 1102–1106 (1979) https://doi.org/10.1029/WR015i005p01102

[10] Lennon, G.P., Liu, P.L.-F., Liggett, J.A.: Boundary integral equation solution to axisymmetric potential flows: 2. recharge and well problems in porous media.

Water Resources Research **15**(5), 1107–1115 (1979) https://doi.org/10.1029/WR015i005p01107

[11] Cooley, R.L.: A finite difference method for unsteady flow in variably saturated porous media: Application to a single pumping well. Water Resources Research **7**(6), 1607–1625 (1971) https://doi.org/10.1029/WR007i006p01607

[12] Dagan, G.: A method of determining the permeability and effective porosity of unconfined anisotropic aquifers. Water Resources Research **3**(4), 1059–1071 (1967) https://doi.org/10.1029/WR003i004p01059

[13] Kipp, K.L. Jr.: Unsteady flow to a partially penetrating, finite radius well in an unconfined aquifer. Water Resources Research **9**(2), 448–462 (1973) https://doi.org/10.1029/WR009i002p00448

[14] Gambolati, G.: Transient free surface flow to a well: An analysis of theoretical solutions. Water Resources Research **12**(1), 27–39 (1976) https://doi.org/10.1029/WR012i001p00027

[15] Di Nucci, C.: Steady free-surface flow in porous media: generalized Dupuit–Fawer equations. Journal of Hydraulic Research **49**(6), 821–823 (2011) https://doi.org/10.1080/00221686.2011.607309

[16] Castro-Orgaz, O.: A new model for soil–water drainage problems. Environmental Fluid Mechanics **11**(4), 427–435 (2011) https://doi.org/10.1007/s10652-010-9196-6

[17] Castro-Orgaz, O., Giráldez, J.V.: Steady-state water table height estimations with an improved pseudo-two-dimensional Dupuit–Forchheimer type model. Journal of Hydrology **438–439**, 194–202 (2012) https://doi.org/10.1016/j.jhydrol.2012.03.023

[18] Di Nucci, C.: A free boundary problem: Steady axisymmetric potential flow. Meccanica **48**, 1805–1810 (2013) https://doi.org/10.1007/s11012-013-9703-1

[19] Di Nucci, C.: Erratum to: A free boundary problem: Steady axisymmetric potential flow. Meccanica **49**, 253 (2014) https://doi.org/10.1007/s11012-013-9841-5

[20] Polubarinova-Kochina, P.Y.: Theory of Ground Water Movement. Princeton University Press, Princeton, NJ (1962)

[21] Shadab, M.A., Hiatt, E., Hesse, M.A.: Pkgui: A gui software for polubarinova-kochina's solutions of steady unconfined groundwater flow. SoftwareX **24**, 101573 (2023) https://doi.org/10.1016/j.softx.2023.101573

[22] Ye, Z., Fan, Q., Huang, S., Cheng, A.: A one-dimensional line element model for transient free surface flow in porous media. Applied Mathematics and

Computation **392**, 125747 (2021) https://doi.org/10.1016/j.amc.2020.125747

[23] Shadab, M.A., Luo, D., Hiatt, E., Shen, Y., Hesse, M.A.: Investigating steady unconfined groundwater flow using physics informed neural networks. Advances in Water Resources **177**, 104445 (2023) https://doi.org/10.1016/j.advwatres.2023.104445

[24] Bourel, C.: Water flow in shallow aquifers without the dupuit hypothesis. Computers & Mathematics with Applications **163**, 165–185 (2024) https://doi.org/10.1016/j.camwa.2024.03.027

[25] Park, Y.-J., Hwang, H.-T., Tanaka, T., Ozutsumi, T., Morita, Y., Mori, K., Berg, S.J., Illman, W.A.: A robust and efficient continuous-differentiable seepage face boundary condition for dynamic groundwater modeling. Water Resources Research **62**(2) (2026) https://doi.org/10.1029/2025WR041547

[26] Castro-Orgaz, O., Giráldez, J.V., Robinson, N.I.: Second-order two-dimensional solution for the drainage of recharge based on Picard's iteration technique: A generalized Dupuit–Forchheimer equation. Water Resources Research **48**(6), 06516 (2012) https://doi.org/10.1029/2011WR011751

[27] Matthew, G.D.: Higher order, one dimensional equations of potential flow in open channels. Proceedings of the Institution of Civil Engineers **91**, 187–201 (1991)

[28] Castro-Orgaz, O., Hager, W.H.: One-dimensional modelling of curvilinear free surface flow: generalized Matthew theory. Journal of Hydraulic Research **52**(1), 14–23 (2014) https://doi.org/10.1080/00221686.2013.834853

[29] Di Nucci, C., Russo Spena, A.: On the steady two-dimensional open channel flow. Journal of Interdisciplinary Mathematics **21**(3), 579–594 (2018) https://doi.org/10.1080/09720502.2015.1086136

[30] Kreyszig, E.: Advanced Engineering Mathematics, 10 edn. John Wiley & Sons, Hoboken, NJ (2011)

[31] Liu, P.L.-F., Wen, J.: Nonlinear diffusive surface waves in porous media. Journal of Fluid Mechanics **347**, 119–139 (1997) https://doi.org/10.1017/S0022112097006472

[32] Jeng, D.-S., Seymour, B.R., Barry, D.A., Parlange, J.-Y., Lockington, D.A., Li, L.: Steepness expansion for free surface flows in coastal aquifers. Journal of Hydrology **309**(1–4), 85–92 (2005) https://doi.org/10.1016/j.jhydrol.2004.11.013